Flux-tube structure from vertical magnetic flux concentrations

A. Brandenburg[1,2], O. Gressel[1], S. Jabbari[1,2], N. Kleeorin[3,1,4], and I. Rogachevskii[3,1,4]

[1] Nordita, KTH Royal Institute of Technology and Stockholm University, Roslagstullsbacken 23, 10691 Stockholm, Sweden
[2] Department of Astronomy, AlbaNova University Center, Stockholm University, 10691 Stockholm, Sweden
[3] Department of Mechanical Engineering, Ben-Gurion University of the Negev, POB 653, Beer-Sheva 84105, Israel
[4] Department of Radio Physics, N. I. Lobachevsky State University of Nizhny Novgorod, Russia

October 9, 2013, Revision: 1.207

ABSTRACT

Context. Strongly stratified hydromagnetic turbulence has previously been found to produce magnetic flux concentrations if the domain is large enough compared with the size of turbulent eddies. Mean-field simulations (MFS) using parameterizations of the Reynolds and Maxwell stresses show a large-scale negative effective magnetic pressure instability and have been able to reproduce many aspects of direct numerical simulations (DNS) regarding growth rate, shape of the resulting magnetic structures, and their height as a function of magnetic field strength. Unlike in the case of an imposed horizontal field, for a vertical one, magnetic flux concentrations of equipartition strength with the turbulence can be reached, resulting in magnetic spots that are reminiscent of sunspots.
Aims. We determine under what conditions magnetic flux concentrations with vertical field occur and what their internal structure is.
Methods. We use a combination of MFS, DNS, and implicit large-eddy simulations (ILES) to characterize the resulting magnetic flux concentrations in forced isothermal turbulence with an imposed vertical magnetic field.
Results. Using DNS, we confirm earlier results that in the kinematic stage of the large-scale instability the horizontal wavelength of structures is about 10 times the density scale height. At later times, even larger structures are being produced in a fashion similar to inverse spectral transfer in helically driven turbulence. Using ILES, we find that magnetic flux concentrations occur for Mach numbers between 0.1 and 0.7. They occur also for weaker stratification and larger turbulent eddies if the domain is wide enough. Using MFS, the size and aspect ratio of magnetic structures are determined as functions of two input parameters characterizing the parameterization of the effective magnetic pressure. DNS, ILES, and MFS show magnetic flux tubes with mean-field energies comparable to the turbulent kinetic energy. These tubes can reach a length of about eight density scale heights. Despite being $\leq 1\%$ equipartition strength, it is important that their lower part is included within the computational domain to achieve the full strength of the instability.
Conclusions. The resulting vertical magnetic flux tubes are being confined by downflows along the tubes and corresponding inflow from the sides, which keep the field concentrated. Application to sunspots remains a viable possibility.

Key words. Sun: sunspots – Sun: magnetic fields – turbulence – magnetohydrodynamics (MHD) – hydrodynamics

1. Introduction

Sunspots and active regions are generally thought to be the result of magnetic fields emerging from deep at the bottom of the solar convection zone (Fan, 2009). Alternatively, solar magnetic activity may be a shallow phenomenon (Brandenburg, 2005). Several recent simulations with realistic physics of solar turbulent convection with radiative transfer have demonstrated the appearance of magnetic flux concentrations either spontaneously (Kitiashvili et al., 2010; Stein & Nordlund, 2012) or as a result of suitable initial conditions (Cheung et al., 2010; Rempel, 2011). There is also the phenomenon of magnetic flux expulsion, which has been invoked as an explanation of the segregation of magneto-convection into magnetized, non-convecting regions and non-magnetized, convecting ones (Tao et al., 1998).

The magneto-hydrothermal structure of sunspots has been studied using the thin flux tube approximation (Spruit, 1981), in which the stability and buoyant rise of magnetic fields in the solar convection zone has been investigated. This theory has been also applied to vertical magnetic flux, which open up toward the surface. An important property of such tubes is the possibility of thermal collapse, caused by an instability that leads to a downward shift of gas and a more compressed magnetic field structure; see Spruit (1979), who adopted a realistic equation of state including hydrogen ionization. However, because of the pres-

ence of turbulent convection, an ad hoc assumption about flow convergence is needed to prevent the tube from disintegrating. This approach also does not capture the generation process, that is now implicitly seen to operate in some of the aforementioned simulations.

To understand the universal physical mechanism of magnetic flux concentrations, which has been argued to be a minimal model of magnetic spot formation in the presence of a vertical magnetic field (Brandenburg et al., 2013), we consider here forced turbulence in a strongly stratified isothermal layer without radiation. In the last few years, there has been significant progress in modelling of the physics of the resulting magnetic flux concentrations in strongly stratified turbulence via the negative effective magnetic pressure instability (NEMPI). The physics behind this mechanism is the suppression of total (hydrodynamic plus magnetic) turbulent pressure by a large-scale magnetic field. At large enough magnetic Reynolds numbers, well above unity, the suppression of the total turbulent pressure can be large, leading to a negative net effect. In particular, it results in an effective magnetic pressure (the sum of non-turbulent and turbulent contributions) becomes negative, so that the large-scale negative effective magnetic pressure instability is excited (Kleeorin et al., 1989, 1990, 1993, 1996; Kleeorin & Rogachevskii, 1994; Rogachevskii & Kleeorin, 2007).

The effects of a large-scale magnetic field on turbulence or turbulent convection have been studied for decades, but in most studies the negative effective magnetic pressure did not cause any unusual effects, because gravity was either neglected or the domain used in direct numerical simulations (DNS) was not big enough to reach sufficient scale separation. However, when domain size and gravitational stratification are big enough, the system can become unstable with respect to NEMPI, which leads to a spontaneous accumulation of magnetic flux. DNS with large scale separation have been used to verify this mechanism for horizontal magnetic fields (Brandenburg et al., 2011; Kemel et al., 2012a, 2013). In that case significant progress has been made in establishing the connection between DNS and related mean-field simulations (MFS). Both approaches show that the resulting magnetic flux concentrations are advected downward in the nonlinear stage of NEMPI. This is because the effective magnetic pressure is negative, so when the magnetic field increases inside a horizontal flux structure, gas pressure and density are locally increased to achieve pressure equilibrium, thus making the effective magnetic buoyancy force negative. This results in a downward flow ('potato-sack' effect). Horizontal mean magnetic fields are advected downward by this flow and never reach much more than a few percent of the equipartition field strength.

The situation is entirely different for vertical magnetic fields. The downflow draws gas downward along magnetic field lines, creating an underpressure in the upper parts, which concentrates the magnetic field to equipartition field strength with respect to the turbulent kinetic energy density (Brandenburg et al., 2013). The resulting magnetic flux concentrations have superficially the appearance of sunspots. For horizontal fields spots can also form and they have the appearance of bipolar regions, as has been found in simulations with a coronal layer above a turbulent region (Warnecke et al., 2013). However, to address the exciting possibility of explaining the occurrence of sunspots by this mechanism, we need to know more about the operation of NEMPI with a vertical magnetic field. In particular, we need to understand how it is possible to obtain magnetic field strengths much larger than the optimal magnetic field strength at which NEMPI is excited. We will do this through a detailed examination of magnetic flux concentrations in MFS, where the origin of flows can be determined unambiguously owing to the absence of the much stronger turbulent convective motions.

We complement our studies with DNS and so-called 'implicit large-eddy' simulations (ILES), which are comparable to DNS in that they aim to resolve the inertial range of the forced turbulence. ILES differ from DNS in that one does not attempt to resolve the dissipation scale, which is numerically expensive due to resolution requirements. In short, ILES are DNS without explicit physical dissipation coefficients. However, unlike large-eddy simulations, no turbulence parameterization model is used at all to represent the unresolved scales. Lacking explicit dissipation, ILES instead relies on suitable properties of the truncation error of the numerical scheme (Grinstein et al., 2005), which guarantees that kinetic and magnetic energies are dissipated near the grid scale. In the finite-volume code NIRVANA (Ziegler, 2004) that we use for ILES here, dissipation occurs in the averaging step of the Godunov scheme. The advantage of the finite-volume scheme is the ability to capture shocks without explicit or artificial viscosity. This allows us to probe the regime of higher Mach numbers without the requirement to adjust the Reynolds number or grid resolution.

Following earlier work of Brandenburg et al. (2011), we will stick to the simple setup of an isothermal layer. This is not only a computational convenience, but it is also conceptually significant, because it allows us to disentangle competing explanations for sunspot and active region formation. One of them is the idea that active regions are being formed and held in place by the more deeply routed supergranulation network at 20–40 Mm depth (Stein & Nordlund, 2012). In a realistic simulation there will be supergranulation and large-scale downdrafts, but NEMPI also produces large-scale downdrafts in nonlinear stage of evolution. However, by using forced turbulence simulations in an isothermal layer, an explanation in terms of supergranulation would not apply.

We emphasize that an isothermal layer can be infinitely extended. Furthermore, the stratification is uniform in the sense that the density scale height is independent of height. Nevertheless, the density varies, so the equipartition magnetic field strength also varies. Therefore, the ratio of the imposed magnetic field strength to the equipartition value varies with height. NEMPI is excited at the height where this ratio is around 3% (Losada et al., 2013). This explains why NEMPI can be arranged to work at any field strength if only the domain is tall enough.

At large domain size, DNS and ILES become expensive and corresponding MFS are an ideal tool to address questions concerning the global shape of magnetic flux concentrations. In that case, significant conceptual simplifications can be achieved by making use of the axisymmetry of the resulting magnetic flux concentrations. We also need to know more about the operation of NEMPI under conditions closer to reality. For example, how does it operate in the presence of larger gravity, larger Mach numbers, and smaller scale separation? This aspect is best being addressed through ILES, where significant dissipation only occurs in shocks.

We consider three-dimensional (3-D) domains and compare in some cases with MFS in two-dimensions (2-D) using axisymmetry or Cartesian geometry. Here, axisymmetry corresponds to vertical tubes while Cartesian geometry corresponds to vertical flux sheets. The MFS provide guidance that is useful for understanding the results of DNS and ILES, so in this paper we begin with MFS, discuss the mechanism of NEMPI and finally focus on the dependencies on gravity, scale separation, and Mach numbers using DNS.

2. Mean-field study of NEMPI

For the analytical study of NEMPI with a vertical field we consider the equations of mean-field MHD for mean magnetic $\overline{\boldsymbol{B}}$ and velocity $\overline{\boldsymbol{U}}$ fields, and mean density $\overline{\rho}$ in the anelastic approximation for low Mach numbers, and for large fluid and magnetic Reynolds numbers,

$$\frac{\partial \overline{\boldsymbol{B}}}{\partial t} = \boldsymbol{\nabla} \times \left(\overline{\boldsymbol{U}} \times \overline{\boldsymbol{B}} - \eta_{\mathrm{t}} \mu_0 \overline{\boldsymbol{J}} \right), \tag{1}$$

$$\overline{\rho} \frac{\mathrm{D}\overline{\boldsymbol{U}}}{\mathrm{D}t} = -\boldsymbol{\nabla}\overline{p}_{\mathrm{tot}} + \mu_0^{-1}(\overline{\boldsymbol{B}} \cdot \boldsymbol{\nabla})\overline{\boldsymbol{B}} + \overline{\rho}\boldsymbol{g} - \nu_{\mathrm{t}}\overline{\rho}\overline{\boldsymbol{Q}}, \tag{2}$$

$$0 = -\boldsymbol{\nabla} \cdot \overline{\rho}\,\overline{\boldsymbol{U}}, \tag{3}$$

where $\mathrm{D}/\mathrm{D}t = \partial/\partial t + \overline{\boldsymbol{U}} \cdot \boldsymbol{\nabla}$ is the advective derivative, $\overline{p}_{\mathrm{tot}} = \overline{p} + p_{\mathrm{eff}}$ is the mean total pressure, $\overline{p}$ is the mean gas pressure,

$$p_{\mathrm{eff}} = (1 - q_{\mathrm{p}})\overline{\boldsymbol{B}}^2/2\mu_0 \tag{4}$$

is the effective magnetic pressure (Kleeorin et al., 1990, 1993, 1996), $\overline{\rho}$ is the mean density, $\overline{\boldsymbol{B}} = \boldsymbol{\nabla} \times \overline{\boldsymbol{A}} + \hat{\boldsymbol{z}}B_0$ is the mean magnetic field with an imposed constant field pointing in the z direction, $\overline{\boldsymbol{J}} = \boldsymbol{\nabla} \times \overline{\boldsymbol{B}}/\mu_0$ is the mean current density, μ_0

is the vacuum permeability, $\boldsymbol{g} = (0, 0, -g)$ is the gravitational acceleration, η_t is turbulent magnetic diffusivity, ν_t is turbulent viscosity,

$$-\overline{\boldsymbol{Q}} = \nabla^2 \overline{\boldsymbol{U}} + \tfrac{1}{3} \boldsymbol{\nabla} \boldsymbol{\nabla} \cdot \overline{\boldsymbol{U}} + 2\overline{\mathsf{S}} \boldsymbol{\nabla} \ln \overline{\rho} \tag{5}$$

is a term appearing in the viscous force with

$$\mathsf{S}_{ij} = \tfrac{1}{2}(\overline{U}_{i,j} + \overline{U}_{j,i}) - \tfrac{1}{3}\delta_{ij}\boldsymbol{\nabla} \cdot \overline{\boldsymbol{U}} \tag{6}$$

being the traceless rate of strain tensor of the mean flow.

We adopt an isothermal equation of state with $p = \rho c_s^2$, where $c_s = \mathrm{const}$ is the sound speed. In the absence of a magnetic field, the hydrostatic equilibrium solution is then given by $\overline{\rho} = \rho_0 \exp(-z/H_\rho)$, where $H_\rho = c_s^2/g$ is the density scale height.

2.1. Analytical estimates of growth rate of NEMPI

We linearize the mean-field equations (1)–(3) around the equilibrium: $\overline{\boldsymbol{U}}_0 = \boldsymbol{0}$, $\overline{\boldsymbol{B}} = \overline{\boldsymbol{B}}_0 = \mathrm{const}$. The equations for small perturbations (denoted by a tilde) can be rewritten in the form

$$\frac{\partial \tilde{\boldsymbol{B}}}{\partial t} = \boldsymbol{\nabla} \times \left(\tilde{\boldsymbol{U}} \times \overline{\boldsymbol{B}}_0 \right), \tag{7}$$

$$\boldsymbol{\nabla} \cdot \tilde{\boldsymbol{U}} = \frac{\tilde{U}_z}{H_\rho}, \tag{8}$$

$$\frac{\partial \tilde{\boldsymbol{U}}}{\partial t} = \frac{1}{\overline{\rho}} \left[\mu_0^{-1}(\overline{\boldsymbol{B}}_0 \cdot \boldsymbol{\nabla})\tilde{\boldsymbol{B}} - \boldsymbol{\nabla}\tilde{p}_{\mathrm{eff}} \right], \tag{9}$$

where

$$\tilde{p}_{\mathrm{tot}} = \tilde{p}_{\mathrm{eff}} = 2\overline{B}_0 \, \tilde{B}_z \left(\frac{\mathrm{d}\mathcal{P}_{\mathrm{eff}}}{\mathrm{d}\beta^2} \right)_{\beta=\beta_0} \equiv 2 \frac{\tilde{B}_z}{\overline{B}_0} \, \delta p_{\mathrm{eff}}. \tag{10}$$

with $\beta = \overline{B}/B_{\mathrm{eq}}$ and $B_{\mathrm{eq}} = \sqrt{\mu_0 \overline{\rho}} \, u_{\mathrm{rms}}$ is the local equipartition field strength, and u_{rms} is assumed to be a constant in the present mean-field study. Here the effective magnetic pressure is written in normalized form as

$$\mathcal{P}_{\mathrm{eff}}(\beta) \equiv p_{\mathrm{eff}}/B_{\mathrm{eq}}^2 = \tfrac{1}{2} \left[1 - q_{\mathrm{p}}(\beta) \right] \beta^2. \tag{11}$$

Here we have neglected all dissipative terms: the turbulent viscosity term in the momentum equation and the turbulent magnetic diffusion term in the induction equation. We use cylindrical coordinates r, φ, z and introduce the magnetic vector potential and stream function:

$$\tilde{\boldsymbol{B}} = \boldsymbol{\nabla} \times (A \mathrm{e}_\varphi), \quad \overline{\rho} \tilde{\boldsymbol{U}} = \boldsymbol{\nabla} \times (\Psi \mathrm{e}_\varphi). \tag{12}$$

Equations (7)–(12) yield

$$\left(\Delta_s + \frac{1}{H_\rho}\nabla_z \right) \frac{\partial^2 \Psi}{\partial t^2} = D^2 \frac{\nabla_z \Psi}{\overline{\rho}}, \tag{13}$$

where $\Delta_s = \Delta - r^{-2}$ and

$$D^2 = \overline{B}_0^2 \left(\nabla_z \Delta_s + \frac{1}{H_\rho}\nabla_z^2 \right) + \frac{2\delta p_{\mathrm{eff}}}{H_\rho}(\Delta_s - \nabla_z^2) \tag{14}$$

are operators, and we have used a standard vertical profile of the fluid density:

$$\overline{\rho} = \overline{\rho}_0 \exp(-z/H_\rho). \tag{15}$$

We introduce a new variable for the axisymmetric problem:

$$\Psi(t, r, z) = \exp(\lambda t) \, \overline{\rho}^{1/2} \, \Phi(r, z). \tag{16}$$

Substituting Eq. (16) into Eq. (13) we obtain the equation for the function $\Phi(r, z)$:

$$\begin{aligned}
\left(\Delta_s - \frac{1}{4H_\rho^2} \right) \lambda^2 \Phi &= v_{\mathrm{A}}^2(z) \left\{ \frac{2\delta p_{\mathrm{eff}}}{\overline{B}_0^2 H_\rho}(\Delta_s - \nabla_z^2) \right. \\
&+ \left[\Delta_s - \nabla_z^2 + \left(\nabla_z + \frac{1}{2H_\rho} \right)\left(\nabla_z + \frac{3}{2H_\rho} \right) \right] \\
&\left. \times \left(\nabla_z + \frac{1}{2H_\rho} \right) \right\} \left(\nabla_z - \frac{1}{2H_\rho} \right) \Phi,
\end{aligned} \tag{17}$$

where $v_{\mathrm{A}}(z) = \overline{B}_0/\sqrt{\mu_0 \overline{\rho}}$ is the mean Alfvén speed. We seek solutions of Eq. (17) in the form

$$\Phi(r, z) = J_1(\sigma r/R) \, \Phi_0(z),$$

where $J_1(x)$ is the Bessel function of the first kind. The equation for the function $\Phi_0(z)$ reads:

$$\begin{aligned}
\left\{ \left((H_\rho \nabla_z)^2 - \frac{1}{4} - \frac{\sigma^2 H_\rho^2}{R^2} \right) \lambda^2 + v_{\mathrm{A}}^2(z) \frac{\sigma^2}{R^2} \left[\frac{2\delta p_{\mathrm{eff}}}{\overline{B}_0^2} \right. \right. \\
+ \left(1 - \frac{R^2}{\sigma^2 H_\rho^2} \left(H_\rho \nabla_z + \frac{1}{2} \right)\left(H_\rho \nabla_z + \frac{3}{2} \right) \right) \\
\left. \left. \times \left(H_\rho \nabla_z + \frac{1}{2} \right) \right] \left(H_\rho \nabla_z - \frac{1}{2} \right) \right\} \Phi_0(z) = 0.
\end{aligned} \tag{18}$$

When $H_\rho \nabla_z \Phi_0/\Phi_0 \ll 1$, the growth rate for NEMPI is given by

$$\lambda = \frac{v_{\mathrm{A}}}{H_\rho} \left[\frac{-\left(\mathrm{d}\mathcal{P}_{\mathrm{eff}}/\mathrm{d}\beta^2 \right)_{\beta=\beta_0} + 3R^2/16\sigma^2 H_\rho^2 - 1/4}{1 + R^2/4\sigma^2 H_\rho^2} \right]^{1/2}. \tag{19}$$

This equation shows that, compare to the simpler case of a horizontal magnetic field, there are additional terms proportional to R^2/H_ρ^2, which could in principle enhance the resulting growth rate of NEMPI. Whether or not this actually happens, and how the resulting magnetic field structure looks like in the nonlinear saturated regime can however only be obtained numerically using MFS.

2.2. MFS models

We now need to make detailed assumptions about the functional form of $p_{\mathrm{eff}}(\beta^2)$. A useful parameterization of q_{p} in Eq. (4) is (Kemel et al., 2012b)

$$q_{\mathrm{p}} = \frac{q_{\mathrm{p}0}}{1 + \beta^2/\beta_{\mathrm{p}}^2} \equiv \frac{\beta_\star^2}{\beta_{\mathrm{p}}^2 + \beta^2}, \tag{20}$$

where $\beta_\star = \sqrt{q_{\mathrm{p}0}}\beta_{\mathrm{p}}$. For consistency with earlier studies, we keep the governing MFS parameters equal to those used in a recent study by Losada et al. (2013). Thus, unless stated otherwise, we use the values

$$q_{\mathrm{p}0} = 32, \quad \beta_{\mathrm{p}} = 0.058 \quad \text{(reference model)}. \tag{21}$$

The mean-field equations are solved numerically without making the anelastic approximation, i.e., we solve

$$\frac{\partial \overline{\rho}}{\partial t} = -\boldsymbol{\nabla} \cdot \overline{\rho}\overline{\boldsymbol{U}} \tag{22}$$

together with the equations for the mean vector potential $\overline{\boldsymbol{A}}$ such that $\overline{\boldsymbol{B}} = \boldsymbol{B}_0 + \boldsymbol{\nabla} \times \overline{\boldsymbol{A}}$ is divergence-free, the mean

velocity $\overline{U}$, and the mean density $\overline{\rho}$, using the PENCIL CODE (http://pencil-code.googlecode.com), which has a mean-field module built in and is used for calculations both in Cartesian and cylindrical geometries. Here $\boldsymbol{B}_0 = (0, 0, B_0)$ is the imposed uniform vertical field. The respective coordinate systems are (x, y, z) and (r, φ, z). In the former case we use periodic boundary conditions in the horizontal directions, $-L_\perp/2 < (x, y) < L_\perp/2$, while in the latter we adopt perfect conductor, free-slip boundary conditions at the side walls at $r = L_r$ and regularity conditions on the axis. On the upper and lower boundaries at $z = z_{\mathrm{top}}$ and $z = z_{\mathrm{bot}}$ we use in both geometries stress-free conditions, i.e. $\hat{\boldsymbol{z}} \times \partial\overline{\boldsymbol{U}}/\partial z = \hat{\boldsymbol{z}} \cdot \overline{\boldsymbol{U}} = \boldsymbol{0}$, and assume the magnetic field to be normal to the boundary, i.e., $\hat{\boldsymbol{z}} \times \overline{\boldsymbol{B}} = \boldsymbol{0}$.

Following earlier work, we display results for the magnetic field either by normalizing with B_0, which is a constant, or by normalizing with B_{eq}, which decreases with height. The strength of the imposed field is often specified in terms of $B_{\mathrm{eq}0} = B_{\mathrm{eq}}(z = 0)$.

2.3. Nondimensionalization

Nondimensional parameters are indicated by tildes and hats, and include $\tilde{B}_0 = B_0/(\mu_0\rho_0 c_s^2)^{1/2}$ and $\tilde{\eta}_{\mathrm{t}} = \eta_{\mathrm{t}}/c_s H_\rho$, in addition to parameters in Eq. (21) characterizing the functional form of $q_{\mathrm{p}}(\beta)$. Additional quantities include $\tilde{k}_{\mathrm{f}} = k_{\mathrm{f}} H_\rho$ and $\hat{k}_{\mathrm{f}} = k_{\mathrm{f}}/k_1$, where a hat is used to indicate nondimensionalization that uses quantities other than c_s and H_ρ, such as $k_1 = 2\pi/L_\perp$, which is the lowest horizontal wavenumber in a domain with horizontal extent $L_\perp$. For example, $\hat{g} = g/c_s^2 k_1$, in nondimensional gravity and $\hat{\lambda} = \lambda H_\rho^2/\eta_{\mathrm{t}}$ is the nondimensional growth rate. It is convenient to quote also $B_0/B_{\mathrm{eq}0}$ with $B_{\mathrm{eq}0} = B_{\mathrm{eq}}(z = 0)$. Note that $B_0/B_{\mathrm{eq}0}$ is larger than $\tilde{B}_0$ by the inverse of the turbulent Mach number, $\mathrm{Ma} = u_{\mathrm{rms}}/c_s$. It is convenient to normalize the mean flow by u_{rms} and denote it by a hat, i.e., $\hat{\overline{U}} = \overline{U}/u_{\mathrm{rms}}$. Likewise, we define $\hat{\overline{B}} = \overline{B}/B_{\mathrm{eq}}$.

In MFS, the value of η_{t} is assumed to be given by $\eta_{\mathrm{t}0} = u_{\mathrm{rms}}/3k_{\mathrm{f}}$. Using the test-field method, Sur et al. (2008) found this to be an accurate approximation of η_{t}. Thus, we have to specify both Ma and $\tilde{k}_{\mathrm{f}}$. In most of our runs we use $\mathrm{Ma} = 0.1$ and $\tilde{k}_{\mathrm{f}} = 33$, corresponding to $\tilde{\eta}_{\mathrm{t}} = 10^{-3}$. Furthermore, k_{f} and H_ρ are in principle not independent of each other either. In fact, mixing length theory suggests $k_{\mathrm{f}} H_\rho \approx 6.5$ (Losada et al., 2013), but it would certainly be worthwhile to compute this quantity from high-resolution convection simulations spanning multiple scale heights. However, in this paper, different values of $k_{\mathrm{f}} H_\rho$ are considered. With these preparations in place, we can now address questions concerning the horizontal wavelength of the instability and the vertical structure of the magnetic flux tubes.

2.4. Aspect ratio of NEMPI

The only natural length scale in an isothermal layer in MFS is H_ρ. It determines the scale of NEMPI. At onset, the horizontal scale of the magnetic field pattern will be a certain multiple of H_ρ. In the following we denote the corresponding horizontal wavenumber of this pattern by $k_\perp$. Earlier work by Kemel et al. (2013) showed that for an imposed horizontal magnetic field we have $k_\perp H_\rho \approx 0.8...1$. This pattern was 2-D in the plane perpendicular to the direction of the imposed magnetic field, corresponding to horizontal rolls oriented along the mean magnetic
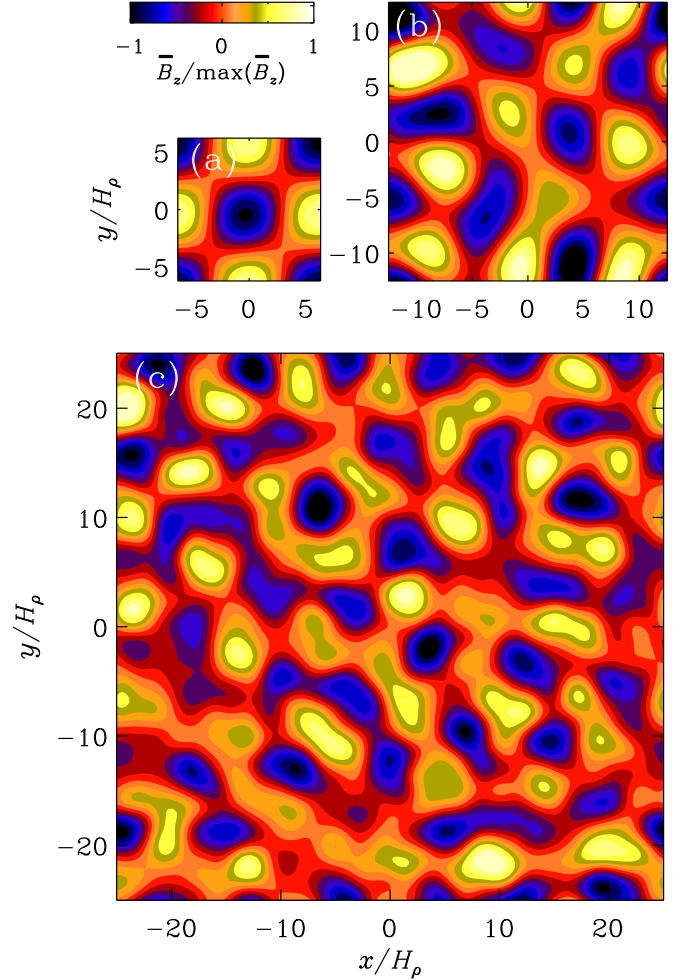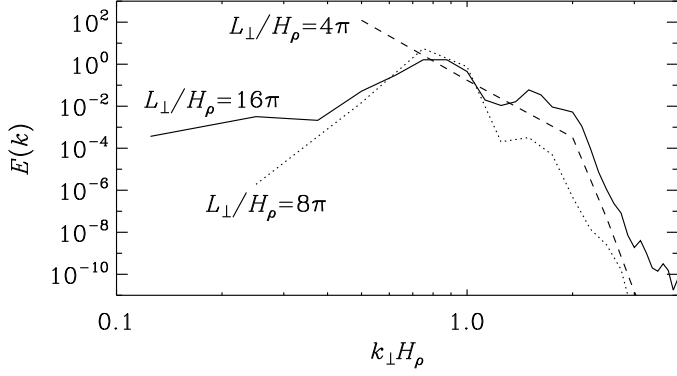

Fig. 1. Horizontal patterns of $\overline{B}_z$ at $z = 0$ from a 3-D MFS during the kinematic growth phase with $B_0/B_{\mathrm{eq}0} = 0.1$ and horizontal extents with (a) $L_\perp/H_\rho = 4\pi$, (b) 8π, and (c) 16π.

field. In the present case of a vertical field, the magnetic perturbations have a cellular pattern with horizontal wavenumber $k_\perp$. To determine the value of $k_\perp H_\rho$ for the case of an imposed vertical magnetic field, we have to ensure that the number of cells per unit area is independent of the size of the domain. In Fig. 1 we compare MFS with horizontal aspect ratios ranging from 2 to 8. We see that the magnetic pattern is fully captured in a domain with normalized horizontal extent $L_\perp/H_\rho = 4\pi$, i.e., the horizontal scale of the magnetic field pattern is twice the value of H_ρ, i.e., $k_x = k_y = H_\rho^{-1}/2$, so that $k_\perp \equiv (k_x^2 + k_y^2)^{1/2} = H_\rho^{-1}/\sqrt{2}$, or $k_\perp H_\rho \approx 0.7$. The value $k_\perp H_\rho \approx 0.7$ is also confirmed by taking a power spectrum of $\overline{B}_z(x, y)$; see Fig. 2, which shows a peak at a similar value.

Comparing the three simulations shown in Fig. 1, we see that a regular checkerboard pattern is only obtained for the smallest domain size; see Fig. 1(a). For larger domain sizes the patterns are always irregular such that a cell of one sign can be surrounded by 3–5 cells of the opposite sign. Nevertheless, in all three cases we have approximately the same number of cells per unit area.

In the nonlinear regime, structures continue to merge and more power is transferred to lower horizontal wavenumbers; see

Fig. 2. Power spectra of $\overline{B}_z$ for different horizontal domain sizes at $z = 0$ from a 3-D MFS during the kinematic growth phase with $B_0/B_{eq0} = 0.1$.
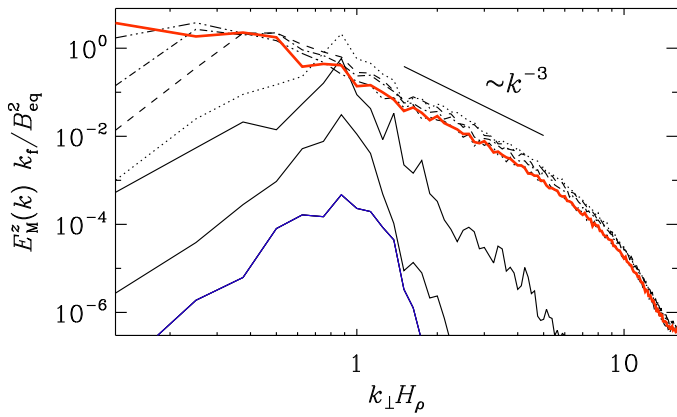

Fig. 3. Time evolution of normalized spectra of B_z from 3-D MFS during the late nonlinear phase at the top of the domain, $k_1 z = \pi$, at normalized times $t\eta_{t0}/H_\rho^2 \approx 5$ (blue), 6, 7, 10, 20, 30, 40, and 50 (red), with $g = c_s^2 k_1$, $B_0/B_{eq0} = 0.1$, and $L_\perp/H_\rho = 16\pi$

Fig. 3. Later in Sect. 3.5 we present similar results also for our DNS.

2.5. Vertical magnetic field profile during saturation

In an isothermal atmosphere, the scale height is constant and there is no physical upper boundary, so we can extend the computation in the z direction at will, although the magnetic pressure will strongly exceed the turbulent pressure at large heights, which can pose computational difficulties. To study the full extent of magnetic flux concentrations, we need a big enough domain. In the following we consider the range $-3\pi \leq z/H_\rho \leq 3\pi$, which results in a density contrast of more than 10^8. To simplify matters, we restrict ourselves in the present study to axisymmetric calculations which are faster than 3-D Cartesian ones.

In Fig. 4 we compare the results for the mean magnetic field profiles for three values of B_0/B_{eq0} ranging from 0.002 to 0.05. These values are smaller than those studied in Sect. 2.4, because in the nonlinear regime and in a deeper domain the structures are allowed to sink by a substantial amount. By choosing B_0/B_{eq0} to be smaller, the tubes are fully contained in our domain. As B_0
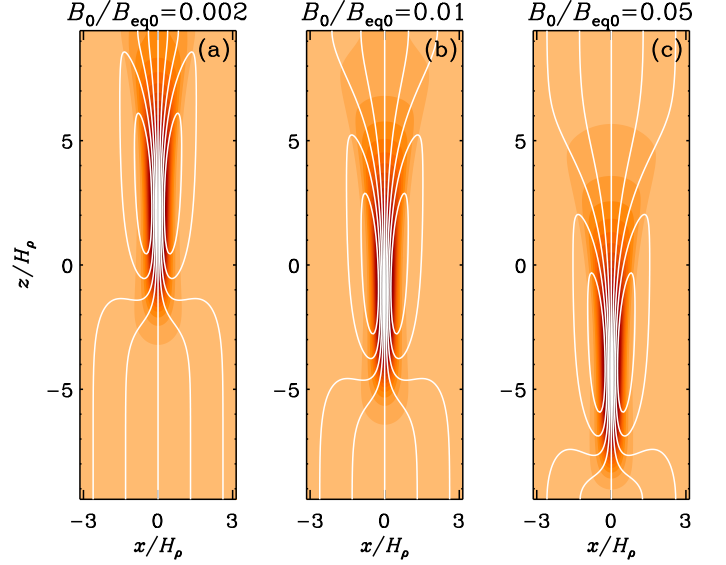
Fig. 4. Comparison of magnetic field profiles from axisymmetric MFS for Runs Bv002/33–Bv05/33 with three values of B_0/B_{eq0} and $\tilde{\eta}_t = 10^{-3}$, corresponding to $k_f H_\rho = 33$.

increases, we expect the position of the magnetic flux tube, z_B, to move downward like

$$z_B = z_{B0} - 2H_\rho \ln(B_0/B_{eq0}), \qquad (23)$$

where $z_{B0} = 2H_\rho \ln \beta_0^{opt}$ is a reference height and

$$\beta_0^{opt} \equiv B_0/B_{eq}(z_B) \approx 0.03...0.06 \qquad (24)$$

is the optimal normalized field strength for NEMPI to be excited (Losada et al., 2013). The validity of Eq. (23) can be verified by Fig. 4, where B_0/B_{eq0} increases by a factor of 25, corresponding to $\Delta z_B = -6.4$.

In all cases, we obtain a slender tube with approximate aspect ratio of 1:8. In other words, the shape of the magnetic field lines is the same for all three values of B_0/B_{eq0}, and just the position of the magnetic flux concentration shifts in the vertical direction. Note in particular that the thickness of structures is always the same. This is different from the nonlinear MFS in Cartesian geometry discussed above, where structures are able to merge. Merging is not really possible in the same way in an axisymmetric container, because any additional structure would correspond to a ring.

The mean flow structure associated with the magnetic flux tube is shown in Fig. 5 for Run Bv05/33 with $B_0/B_{eq0} = 0.05$. We find inflow into the tube along field lines at large heights and outflow at larger depth. The vertical component of the flow in the tube points always downward, i.e., there is no obvious effect from positive magnetic buoyancy. The maximum downflow speed is about $0.27u_{rms}$, so it is subdominant compared with the turbulent velocity, but this could be enough to cause a noticeable temperature change in situations where the energy equation is solved.

The resulting magnetic field lines look roughly similar to those of the DNS with an imposed vertical magnetic field (Brandenburg et al., 2013). In DNS, however, the thickness of the magnetic flux tube is larger than in the MFS by about a factor of three. This discrepancy could be explained if the actual value of η_t was in fact larger than the estimate given by η_{t0}. We return to this possibility in Sect. 3.5. Alternatively, it might be
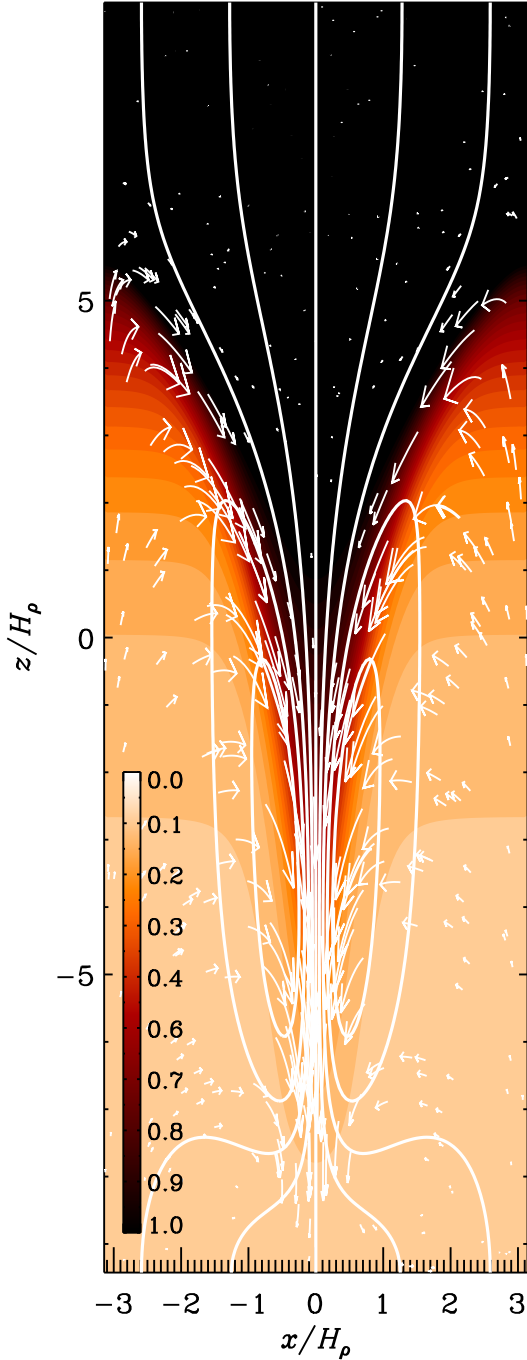
Fig. 5. $\overline{B}_z/B_{eq}$ together with field lines and flow vectors from MFS, for Run Bv05/33 with $B_0/B_{eq0} = 0.05$. The flow speed varies from $-0.27u_{rms}$ (downward) to $0.08u_{rms}$ (upward).

related to the possibility that the coefficients in Eq. (21) could actually be different.

The time evolution of the vertical magnetic field profiles, $\overline{B}_z^{max}/B_0$ and $\overline{B}_z^{max}/B_{eq}(z)$, are shown in Fig. 6 at different times for the case $B_0/B_{eq0} = 0.05$, corresponding to Fig. 4(c). Here, we also show the time evolution of the corresponding profiles of $\mathcal{P}_{eff}(z)$ and $(-d\mathcal{P}_{eff}/d\ln\beta^2)^{1/2}$. In the kinematic regime, the peak of the latter quantity is a good indicator of the peak of the eigenfunction (Kemel et al., 2013). In the present case, the magnetic field in the kinematic phase peaks at a height
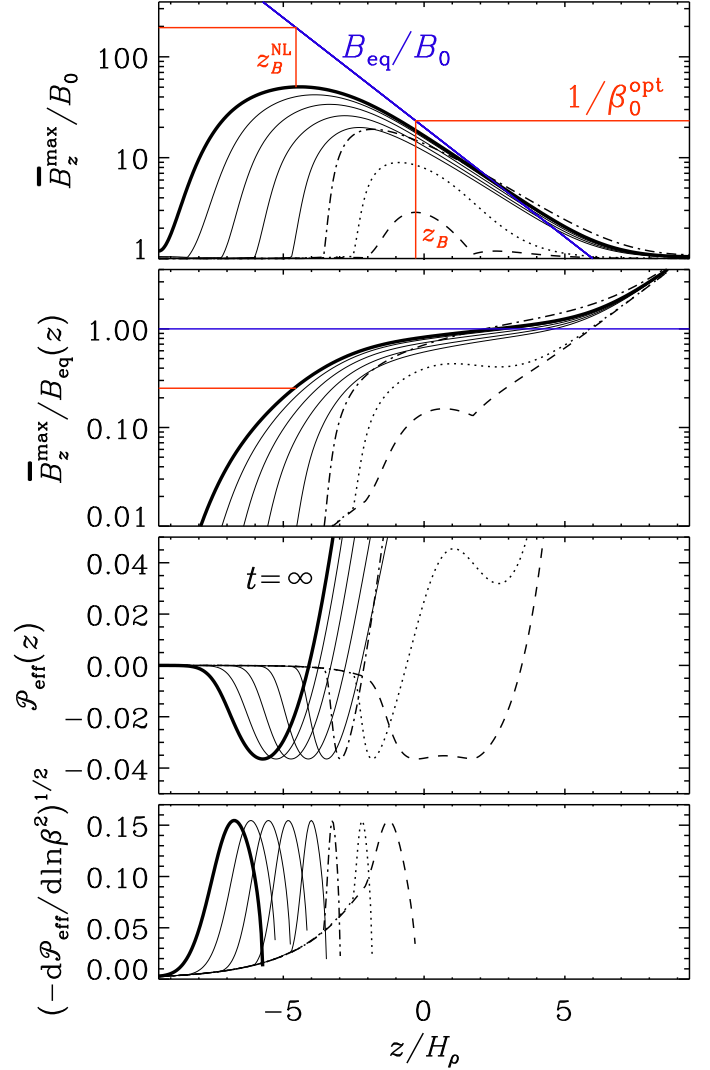

Fig. 6. Time evolution of normalized vertical magnetic field profiles, (a) $\overline{B}_z^{max}/B_0$ together with $B_{eq}(z)/B_0$ (shown by blue line), (b) $\overline{B}_z^{max}/B_{eq}(z)$, as well as (c) $\mathcal{P}_{eff}(z)$ and (d) $(-d\mathcal{P}_{eff}/d\ln\beta^2)^{1/2}$, from a MFS for Run Bv05/33 with $B_0/B_{eq0} = 0.05$ at $t/\tau_{td} = 2.9$ (dashed), 3 (dotted), 3.1 (dash-dotted), 3.3, 3.7, 4.2., 5, and 50 (thick solid line). The blue solid lines indicate $B_{eq}(z)$, normalized by (a) B_0 and (b) by itself (corresponding thus to unity). The red lines indicate the locations z_B and z_B^{NL}, as well as relevant intersections with normalized values of $\overline{B}_z^{max}$ and B_{eq}.

z_B that is given by the condition (24). According to the MFS of Losada et al. (2013), this condition is approximately the same for vertical and horizontal fields. Looking at Fig. 6 for $B_0/B_{eq0} = 0.05$, we see that at $z/H_\rho \approx -0.5$ we have $B_{eq}/B_0 \approx 33$, which agrees with Eq. (24). However, unlike the case of a horizontal magnetic field, where in the kinematic phase the mean field was found to peak at a height below that where $(-d\mathcal{P}_{eff}/d\ln\beta^2)^{1/2}$ peaks, we now see that the field peaks above that position.

As NEMPI begins to saturate, the peak of $\overline{B}_z^{max}$ moves further down to $z = z_B^{NL} \approx -5\,H_\rho$ during the next one or two turbulent diffusive times. By that time, $\overline{B}_z^{max}$ has reached values up to $\overline{B}_z^{max}/B_0 \approx 50$. At that depth, $\overline{B}_z^{max}/B_{eq}(z)$ is about 0.25, but this quantity continues to increase with height and reaches super-equipartition values at $z/H_\rho \approx 3$ (second panel of Fig. 6).
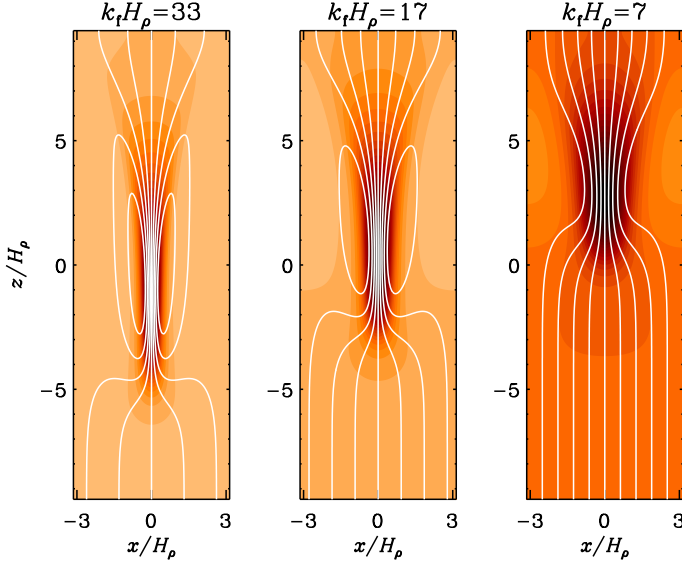
Fig. 7. Comparison of magnetic field profiles from an axisymmetric MFS for Runs Bv01/33–Bv01/7 with $B_0/B_{\mathrm{eq0}} = 0.01$ and three values of $k_{\mathrm{f}}H_\rho$.
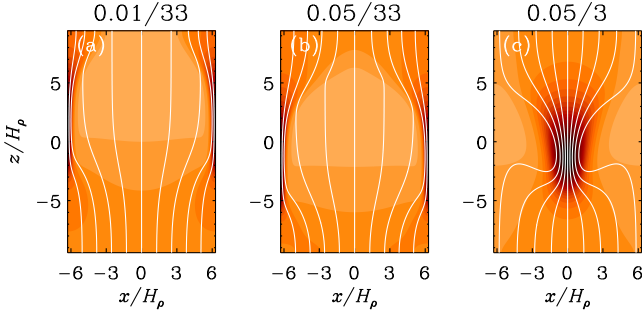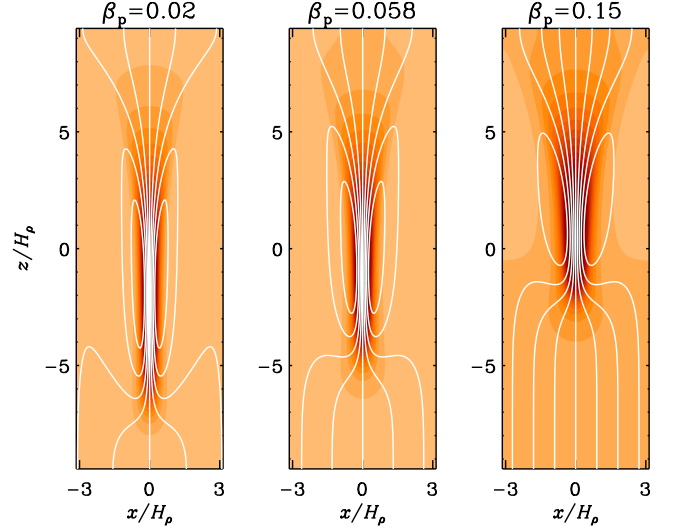

Fig. 8. Comparison of magnetic field structure in axisymmetric MFS. (a) Run 0.01/33 with $B_0/B_{\mathrm{eq0}} = 0.01$ and (b) Run 0.05/33 with $B_0/B_{\mathrm{eq0}} = 0.05$, both with $k_{\mathrm{f}}H_\rho = 33$. The flow speeds vary from $-0.27u_{\mathrm{rms}}$ to $0.08u_{\mathrm{rms}}$ in both cases. (c) Run 0.05/3 with $B_0/B_{\mathrm{eq0}} = 0.05$ and $k_{\mathrm{f}}H_\rho = 3$. The flow speed varies from $-0.23u_{\mathrm{rms}}$ to $0.07u_{\mathrm{rms}}$.

2.6. Smaller scale separation

In MFS, as noted above, the wavenumber of turbulent eddies, k_{f}, enters the expression for the turbulent diffusivity via $\eta_{\mathrm{t}} \approx u_{\mathrm{rms}}/3k_{\mathrm{f}}$, and thus $\tilde{\eta}_{\mathrm{t}} \approx \mathrm{Ma}/3\tilde{k}_{\mathrm{f}}$, so we have

$$\tilde{k}_{\mathrm{f}} \equiv k_{\mathrm{f}}H_\rho = H_\rho^2/3\tau\eta_{\mathrm{t}} = \mathrm{Ma}/3\tilde{\eta}_{\mathrm{t}}, \tag{25}$$

where $\tau = H_\rho/u_{\mathrm{rms}}$ is the turnover time per scale height. When u_{rms} is kept unchanged, smaller scale separation implies a decrease of $\tilde{k}_{\mathrm{f}}$, i.e., the size of turbulent eddies in the domain is increased. Earlier work indicated that the growth rate of the instability for horizontal magnetic field decreases with decreasing $\tilde{k}_{\mathrm{f}}$ (Brandenburg et al., 2012). However, we do not know whether this also causes a change in the spot diameter, which would be plausible, or a change in the depth at which NEMPI occurs. In our MFS we have chosen $\mathrm{Ma} = 0.1$ and $\tilde{\eta}_{\mathrm{t}}$ corresponds to $\tilde{k}_{\mathrm{f}} \approx 33$. For $\tilde{\eta}_{\mathrm{t}} = 5 \times 10^{-3}$ we have $\tilde{k}_{\mathrm{f}} \approx 6$, which is about the smallest scale separation for which NEMPI is still possible in this geometry; see Fig. 7. Interestingly, as $\tilde{k}_{\mathrm{f}}$ is decreased, the location of the flux tube structure moves upward.

Fig. 9. Comparison of magnetic field structure in axisymmetric MFS for Runs Bu01/33–Bw01/33 with three values of β_{p}.

This can be understood as a consequence of enhanced turbulent diffusion, which makes the flux tubes less concentrated, so the magnetic field is weaker, but weaker magnetic field sinks less than stronger fields.

Even for $k_{\mathrm{f}}H_\rho \approx 3$ it is still possible to find NEMPI in MFS, but, as we have seen, the flux tube moves upward and becomes thicker. To accommodate for this change, we need to increase the diameter of the domain and, in addition, we would either need to extend it in the upward direction or increase the magnetic field strength to move the tube back down again; cf. Fig. 4. We choose here the latter. In Fig. 8 we show three cases for a wider box. In the first two runs (referred to as '0.01/33' and '0.05/33') we keep the scale separation ratio the same as before, i.e. $\tilde{k}_{\mathrm{f}} = 33$, and increase B_0/B_{eq0} from 0.01 to 0.05, while in the third case we keep $B_0/B_{\mathrm{eq0}} = 0.05$ and decrease $\tilde{k}_{\mathrm{f}}$ to 3. We increase the magnetic field by a factor of 5 so as to keep the structure within the computational domain. In the first case, the natural separation between tubes would be too small for this large cylindrically symmetric container. By contrast, in a 3-D Cartesian domain, a second downdraft would form, which is not possible in cylindrical geometry. Instead, a downdraft develops on the outer rim of the container. On the other hand, if $\tilde{k}_{\mathrm{f}}$ is decreased and thus $\tilde{\eta}_{\mathrm{t}}$ increased, a single downdraft is again possible, as shown in Fig. 8(b), suggesting that the horizontal scale of structures is also increased as $\tilde{\eta}_{\mathrm{t}}$ is increased. We see that the tube can now attain significant diameters. Its height remains unchanged, so the aspect ratio of the structure is decreased as the scale separation ratio is decreased.

2.7. Parameter sensitivity

It is also important to know the dependence of the solutions on changes of the parameters β_{p} and $\beta_\star$ that determine the function q_{p}. In Figs. 9–11 we present results where we change either β_{p} or $\beta_\star$, respectively. Characteristic properties of these solutions are summarized in Table 1. Runs Ov002/33–Ov05/33 are 2-D Cartesian while all other ones are 2-D axisymmetric. In addition to β_{p} and $\beta_\star$, we also list the values of $q_{\mathrm{p0}} = \beta_\star^2/\beta_{\mathrm{p}}^2$, as well as

Table 1. Survey of axisymmetric MFS giving normalized mean field strengths, mean flow speeds, and other properties for different values of β_0, $\beta_\star$, β_p, $\tilde{k}_f$, and $\tilde{z}_{bot}$. In all cases we have $k_1 H_\rho = 1$, so $\tilde{k}_f = \hat{k}_f$. The asterisk indicates that the domain was clipped at $z = 0$.

Run	β_0	q_{p0}	$\beta_\star$	β_p	β_{min}	$\mathcal{P}_{eff}^{min}$	$\tilde{k}_f$	$\tilde{z}_{bot}$	$\hat{\overline{B}}_z^{max}$	$\hat{\overline{U}}_z^{min}$	$\hat{\overline{U}}_z^{max}$	$\tilde{z}_B$	$\tilde{z}_B^{NL}$	$\tilde{Z}_b$	$\tilde{Z}_t$	$\tilde{R}$	A
Ov002/33	0.002	32	0.33	0.058	0.125	-0.036	33	-3π	52	-0.27	0.03	8.3	4.8	3.5	4.6	0.27	17
Ov01/33	0.01	32	0.33	0.058	0.125	-0.036	33	-3π	52	-0.27	0.08	5.0	1.6	3.6	4.3	0.27	16
Ov05/33	0.05	32	0.33	0.058	0.125	-0.036	33	-3π	51	-0.27	0.08	1.7	-1.7	3.7	4.3	0.27	16
Bv002/33	0.002	32	0.33	0.058	0.125	-0.036	33	-3π	52	-0.27	0.03	7.9	2.0	3.1	4.1	0.35	12
Bv01/33	0.01	32	0.33	0.058	0.125	-0.036	33	-3π	52	-0.27	0.08	3.9	-1.2	3.1	4.1	0.35	12
Bv05/33	0.05	32	0.33	0.058	0.125	-0.036	33	-3π	51	-0.27	0.08	1.8	-4.4	3.0	4.1	0.35	12
Bv01/33	0.01	32	0.33	0.058	0.125	-0.036	33	-3π	52	-0.27	0.08	4.8	-1.2	3.1	4.1	0.35	12
Bv01/17	0.01	32	0.33	0.058	0.125	-0.036	17	-3π	25	-0.27	0.08	4.9	0.3	2.8	4.1	0.50	8
Bv01/7	0.01	32	0.33	0.058	0.125	-0.036	7	-3π	8	-0.23	0.07	4.7	2.7	2.4	3.8	0.95	4
Bu01/33	0.01	270	0.33	0.02	0.079	-0.048	33	-3π	69	-0.35	0.10	4.5	-2.1	4.0	4.5	0.30	15
Bv01/33	0.01	32	0.33	0.058	0.125	-0.036	33	-3π	52	-0.27	0.08	4.8	-1.2	3.1	4.1	0.35	12
Bw01/33	0.01	4.8	0.33	0.15	0.164	-0.016	33	-3π	25	-0.15	0.05	5.4	0.3	2.2	3.8	0.50	8
Av01/33	0.01	12	0.2	0.058	0.091	-0.010	33	-3π	22	-0.13	0.04	4.3	-0.3	2.3	3.8	0.55	7
Bv01/33	0.01	32	0.33	0.058	0.125	-0.036	33	-3π	52	-0.27	0.08	4.8	-1.2	3.1	4.1	0.35	12
Cv01/33	0.01	74	0.5	0.058	0.160	-0.097	33	-3π	91	-0.47	0.09	5.4	-1.7	3.5	4.3	0.25	17
Av01/33*	0.01	12	0.2	0.058	0.091	-0.010	33	0	11	-0.07	0.04	4.2	1.6	1.4	3.4	0.85	4
Bv01/33*	0.01	32	0.33	0.058	0.125	-0.036	33	0	21	-0.15	0.08	4.7	1.5	1.3	3.3	0.60	5
Cv01/33*	0.01	74	0.5	0.058	0.160	-0.097	33	0	33	-0.26	0.10	5.3	1.4	1.2	3.2	0.50	6
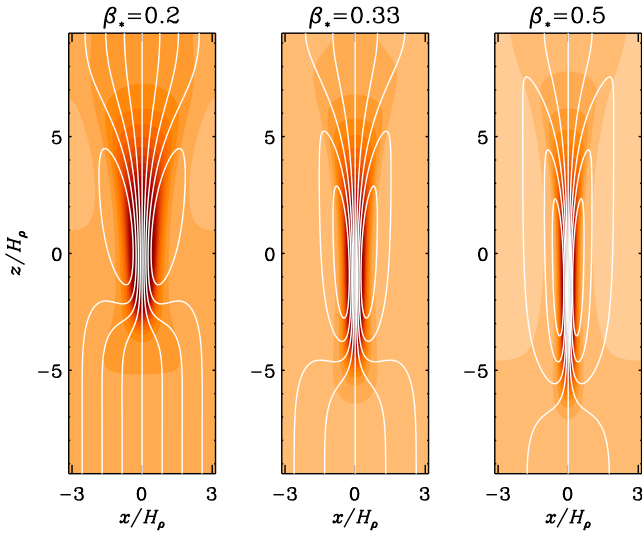
Fig. 10. Comparison of magnetic field structure in axisymmetric MFS for Runs Av01/33–Cv01/33 three values of $\beta_\star$.
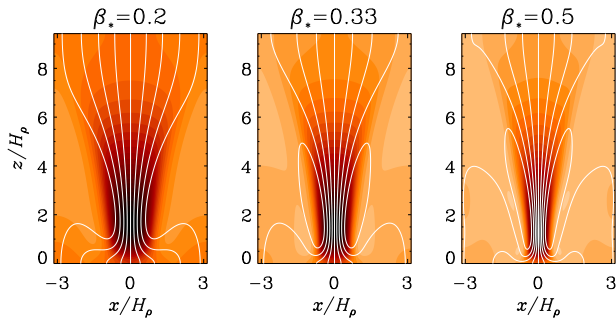
Fig. 11. Comparison of magnetic field structure in axisymmetric MFS for Runs Av–Cv01/33* with three values of $\beta_\star$ in a domain that is cut short from below.

the minimum position of the $\mathcal{P}_{eff}(\beta)$ curve, namely (cf. Kemel et al., 2012b)

$$\mathcal{P}_{eff}^{min} = -\tfrac{1}{2}(\beta_\star^2 - \beta_p^2)^2, \quad \beta_{min} = \left(\beta_p \sqrt{-2\mathcal{P}_{eff}^{min}}\right)^{1/2}. \quad (26)$$

The main output parameters include the maximum normalized vertical field in the tube $\hat{\overline{B}}_z^{max} = \overline{B}_z^{max}/B_0$, the minimum and maximum normalized velocities, $\hat{\overline{U}}_z^{min/max} = \overline{U}_z^{min/max}/u_{rms}$, the normalized maximum magnetic field positions in the linear and nonlinear regimes, $\tilde{z}_B = z_B/H_\rho$ and $\tilde{z}_B^{NL} = z_B^{NL}/H_\rho$, respectively, the similarly normalized positions where $\overline{B}_z$ has dropped by $1/e$ of its maximum at the bottom, $\tilde{Z}_b$, at the top $\tilde{Z}_t$, and to the side $\tilde{R}$, as well as the aspect ratio, $A = Z_t/R$.

We find that structures become taller when β_p is small and $\beta_\star$ large, and they become shorter and fatter when β_p is large and $\beta_\star$ small. Thus, thicker structures, as indicated by the DNS of Brandenburg et al. (2013), could also be caused by larger values of β_p or smaller values of $\beta_\star$. When the domain is clipped at $z = 0$, flux concentrations cannot fully develop. The structures are fatter and less strong.

3. DNS and ILES studies

In the MFS discussed above, we have ignored the possibility of other terms in the parameterization of the mean-field Lorentz force. While this seems to capture the essence of earlier DNS (Brandenburg et al., 2013), this parameterization might not be accurate or sufficient in all respects. It is therefore useful to perform DNS to see how the results depend on scale separation, gravitational stratification, and Mach number.

3.1. DNS and ILES models

We have performed direct numerical simulations using both the PENCIL CODE (http://pencil-code.googlecode.

Table 2. Summary of DNS at varying $\tilde{B}_0$, and fixed values of $\tilde{\eta}_0 = 2 \times 10^{-4}$, $\mathrm{Pr}_M = 0.5$, $\mathrm{Re} \approx 38$, $\mathrm{Ma} \approx 0.1$, $\hat{g} = 1$, $\hat{k}_{\mathrm{f}} = 30$, $\tau_{\mathrm{td}}/\tau_{\mathrm{to}} \approx 2700$, using 256^3 mesh points. In all cases the number of spots is unity. The positions $\tilde{z}_B^{\mathrm{NL}}$ agree with those marked in Fig. 12.

$\hat{B}_0$	Re	Re$_M$	Ma	$\hat{B}_z$	$\hat{\overline{B}}_z$	$\tilde{R}$	$\tilde{z}_B^{\mathrm{NL}}$
0.0005	39	19	0.12	1.81	0.36	0.13	3.1
0.0010	39	19	0.12	2.68	1.00	0.11	1.8
0.0020	38	19	0.11	2.45	0.87	0.17	1.4
0.0050	37	18	0.11	3.47	1.25	0.22	−0.5
0.0100	35	18	0.11	3.95	1.49	0.29	−1.2
0.0200	31	16	0.09	4.21	1.26	0.45	−π

com) and NIRVANA (`http://nirvana-code.aip.de/`). Both codes are fully compressible and are here used with an isothermal equation of state with $p = \rho c_{\mathrm{s}}^2$, where $c_{\mathrm{s}} = \mathrm{const}$ is the sound speed. The background stratification is then also isothermal. Turbulence is driven using volume forcing given by a function $\boldsymbol{f}$ that is δ correlated in time and monochromatic in space. It consists of random non-polarized waves whose direction and phase change randomly at each time step.

In DNS we solve the equations for the velocity $\boldsymbol{U}$, the magnetic vector potential $\boldsymbol{A}$, and the density ρ,

$$\frac{\mathrm{D}\boldsymbol{U}}{\mathrm{D}t} = -c_{\mathrm{s}}^2 \boldsymbol{\nabla} \ln \rho + \frac{1}{\rho} \boldsymbol{J} \times \boldsymbol{B} + \boldsymbol{f} + \boldsymbol{g} + \boldsymbol{F}_\nu, \quad (27)$$

$$\frac{\partial \boldsymbol{A}}{\partial t} = \boldsymbol{U} \times \boldsymbol{B} + \eta \nabla^2 \boldsymbol{A}, \quad (28)$$

$$\frac{\partial \rho}{\partial t} = -\boldsymbol{\nabla} \cdot \rho \boldsymbol{U}, \quad (29)$$

where $\mathrm{D}/\mathrm{D}t = \partial/\partial t + \boldsymbol{U} \cdot \boldsymbol{\nabla}$ is the advective derivative, η is the magnetic diffusivity due to Spitzer conductivity of the plasma, $\boldsymbol{B} = \boldsymbol{B}_0 + \boldsymbol{\nabla} \times \boldsymbol{A}$ is the magnetic field, $\boldsymbol{B}_0 = (0, 0, B_0)$ is the imposed uniform vertical field, $\boldsymbol{J} = \boldsymbol{\nabla} \times \boldsymbol{B}/\mu_0$ is the current density, μ_0 is the vacuum permeability, $\boldsymbol{F}_\nu = \boldsymbol{\nabla} \cdot (2\nu\rho\mathbf{S})$ is the viscous force. The turbulent rms velocity is approximately independent of z. Boundary conditions are periodic in the horizontal directions (so vertical magnetic flux is conserved), and stress free on the upper and lower boundaries where the magnetic field is assumed to be vertical, i.e., $B_x = B_y = 0$. In the ILES we solve the induction equation directly for $\boldsymbol{B}$, ignore the effects of explicit viscosity and magnetic diffusivity and use an approximate Riemann solver to keep the code stable and to dissipate kinetic and magnetic energies at small scales.

The simulations are characterized by specifying a forcing amplitude, which results in a certain rms velocity, u_{rms}, and hence in a certain Mach number. Furthermore, the values of ν and η are quantified through the fluid and magnetic Reynolds numbers, $\mathrm{Re} = u_{\mathrm{rms}}/\nu k_{\mathrm{f}}$ and $\mathrm{Re}_M = u_{\mathrm{rms}}/\eta k_{\mathrm{f}}$, respectively. Their ratio is the magnetic Prandtl number, $\mathrm{Pr}_M = \nu/\eta$.

An important diagnostics is the vertical magnetic field, B_z, at some horizontal layer. In particular, we use here the Fourier-filtered field, $\overline{B}_z$, which is obtained by removing all components with wave numbers larger than 1/6 of the forcing wavenumber k_{f}. This corresponds to a position in the magnetic energy spectrum where there is a local minimum, so we have some degree of scale separation between the forcing scale and the scale of the spot. We return to this in Sect. 3.5. To identify the magnetic field in the magnetic flux tube, we take the maximum of $\overline{B}_z$, either at each height at one time, which is referred to as $\overline{B}_z^{\mathrm{max}}(z)$, or
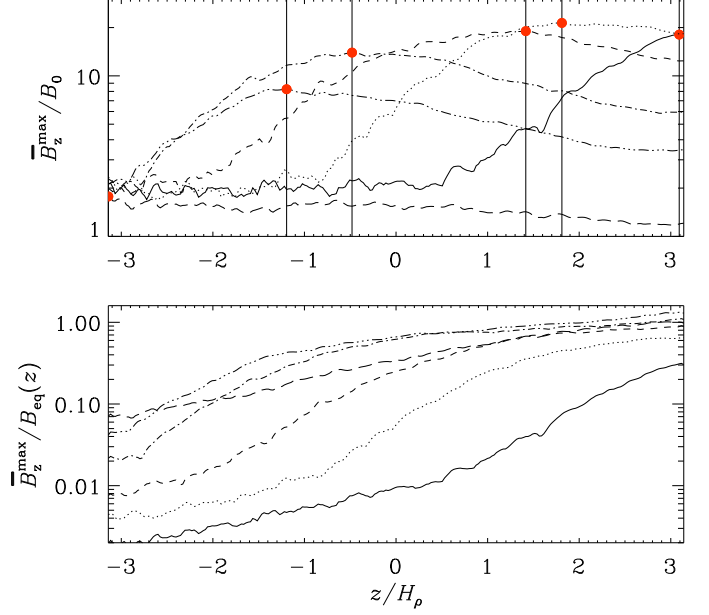

Fig. 12. Normalized vertical magnetic field profiles from DNS, $\overline{B}_z^{\mathrm{max}}/B_0$ (top) and $\overline{B}_z^{\mathrm{max}}/B_{\mathrm{eq}}(z)$ (bottom) for the six values of $B_0/B_{\mathrm{eq}0}$ listed in Table 2. The red dots mark the maxima of $\overline{B}_z^{\mathrm{max}}/B_0$ at positions $\tilde{z}_B^{\mathrm{NL}}$.
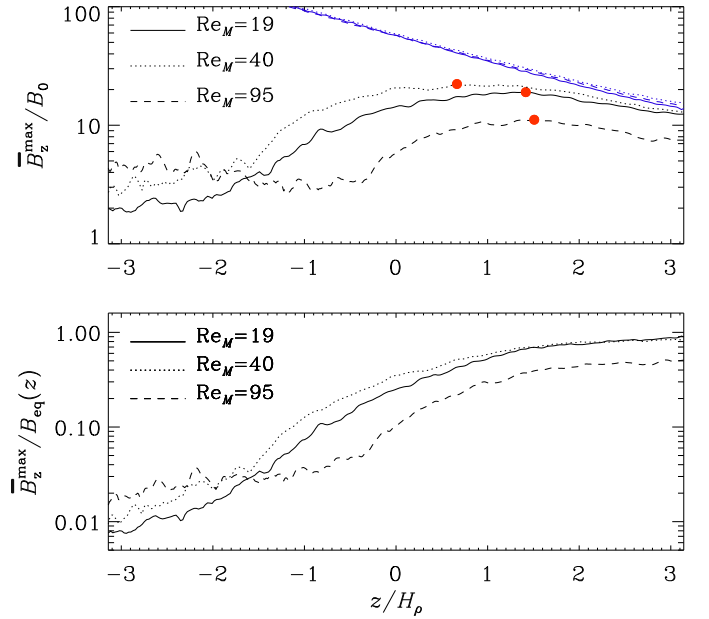
Fig. 13. Similar to Fig. 12, but for DNS Runs A30/1–C30/1 listed in Table 4. In the upper panel, the blue lines denote $B_{\mathrm{eq}}(z)/B_0$.

in the top layer at all times. The latter is used to determine the growth rate of the instability.

When comparing results for different values of g, it is convenient to keep the typical density at the surface the same. Since our hydrostatic stratification is given by Eq. (15), this is best done by letting the domain terminate at $z = 0$ and to consider the range $-L_z \leq z \leq 0$. In most of the cases we consider $L_z = \pi/k_1$, although this might in hindsight be a bit short in some cases. For comparison with earlier work of Brandenburg et al. (2013), we also present models in a domain $-\pi \leq k_1 z \leq \pi$.
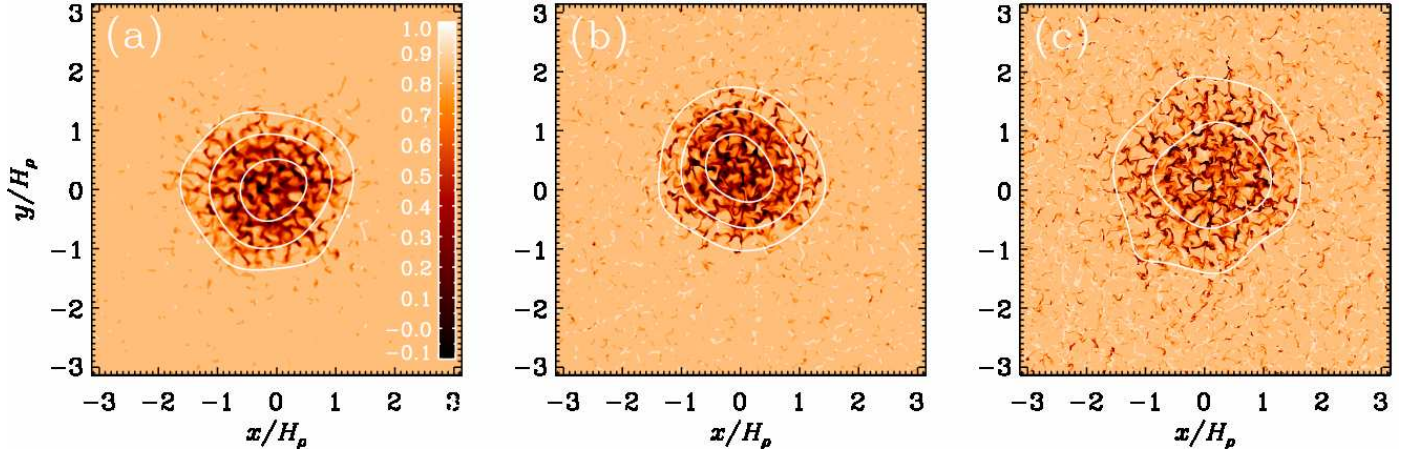
Fig. 14. Magnetic field configuration at the upper surface for DNS Runs A30/1–C30/1 at three values of the magnetic Reynolds number. The white contours represent the Fourier-filtered with $k_\perp \leq k_{\rm f}/6$; their levels correspond to $\overline{B}_z^{\rm max}/B_{\rm eq}(z_{\rm top}) = 0.05$, 0.2, and 0.4.

Table 3. Summary of DNS at varying $\Pr_M$, and fixed values of $\tilde{B}_0 = 0.002$, $\mathrm{Re}_M \approx 20\text{--}40$, Ma ≈ 0.1, $\hat{g} = 1$, $\hat{k}_{\rm f} = 30$, $\tau_{\rm td}/\tau_{\rm to} \approx 2700$, using 256^3 mesh points. In all cases the number of spots is unity.

$\tilde{\nu}$	$\Pr_M$	Re_M	Ma	$\hat{\lambda}$	$\hat{B}_z$	$\hat{\overline{B}}_z$	$\tilde{R}$
4×10^{-5}	0.2	20	0.12	5.18	1.87	0.19	0.36
1×10^{-4}	0.5	19	0.11	1.33	2.45	0.87	0.17
2×10^{-4}	1	17	0.10	1.66	2.76	0.84	0.17
4×10^{-4}	2	14	0.08	1.46	2.78	0.64	0.20
5×10^{-4}	5	25	0.07	0.10	2.66	0.22	0.34
1×10^{-3}	10	19	0.06	0.04	2.87	0.28	0.30
5×10^{-4}	10	45	0.07	0.04	2.96	0.22	0.34

Table 4. Summary of DNS at varying Re and Re_M, and fixed values of $\tilde{B}_0 = 0.002$, $\Pr_M = 0.5$, $k_1 H_\rho = 1$, and $k_{\rm f} H_\rho = 30$.

Run	Re	Re_M	Ma	$\hat{B}_z$	$\hat{\overline{B}}_z$	$\tilde{R}$	Resol.
A30/1	38	19	0.11	2.45	0.87	0.17	256^3
B30/1	80	40	0.12	3.30	1.02	0.16	512^3
b30/1	200	40	0.12	3.45	1.10	0.15	512^3
C30/1	190	95	0.11	3.47	0.71	0.19	1024^3

3.2. Magnetic field dependence

In Table 2 and Fig. 12 we compare results for six values of $\tilde{B}_0 = B_0/(\mu_0\rho_0 c_{\rm s0}^2)^{1/2}$. These models are the same as those discussed in Brandenburg et al. (2013), where visualizations are shown for all six cases. Increasing $\tilde{B}_0$ leads to a decrease in the Mach number Ma and hence to a mild decline of Re and Re_M for $\tilde{B}_0 > 0.01$, corresponding to $B_0/B_{\rm eq0} > 0.1$. There is a slight increase of $\tilde{B}_z^{\rm max}$, while $\tilde{\overline{B}}_z^{\rm max}$ remains of the order of unity. This is the case even for the largest value, $\tilde{B}_0 = 0.02$, when NEMPI is completely suppressed and there is no distinct maximum of $\overline{B}_z^{\rm max}/B_0$ in the upper panel of Fig. 12. This is why the visualization in Brandenburg et al. (2013) was featureless for $\tilde{B}_0 = 0.02$, even though $\tilde{B}_z/B_{\rm eq}(z) \approx 1$ at $z = z_{\rm top}$. Moreover, while $\tilde{B}_z^{\rm max}$ shows only a slight increase, the nondimensional radius of the spot increases from 0.1 to about 0.4 as $\tilde{B}_0$ is increased.

3.3. Magnetic Prandtl number dependence

The results for different values of $\Pr_M$ are summarized in Table 3. It turns out that for $\Pr_M \geq 5$, no magnetic flux concentrations are produced. We recall that analysis based on the quasilinear approach (which is valid for small fluid and magnetic Reynolds numbers) has shown that for $\Pr_M \geq 8$ and $\mathrm{Re}_M \ll 1$, no negative effective magnetic pressure is possible (Rüdiger et

al., 2012; Brandenburg et al., 2012). Because of this, most of the earlier work used $\Pr_M = 0.5$ so as to stay below unity in the hope that this would be a good compromise between $\Pr_M$ being small and Re_M still being reasonably large. In fact, it now turns out that the difference in $\overline{B}_z^{\rm max}$ for $\Pr_M = 1$ and $1/2$ be negligible, and even for $\Pr_M = 2$ the decline in $\overline{B}_z^{\rm max}$ is still small. For $\Pr_M = 0.2$, on the other hand, we find a large value of $\hat{\lambda}$, but a low saturation level. Again, this might be explained by the fact that the domain is not deep enough in the z direction, which can suppress NEMPI. Alternatively, the resolution of 256^3 might not be sufficient to resolve the longer inertial range for smaller magnetic Prandtl numbers. In Sect. 3.4 we present another case with $\Pr_M = 0.2$ where both the resolution and the Reynolds numbers are doubled, and $\overline{B}_z^{\rm max}$ is again large.

3.4. Reynolds number dependence

Increasing Re_M from 19 to 95, we see some changes; see Table 4. There is first a small increase of $\overline{B}_z^{\rm max}/B_{\rm eq}(z)$ from 0.87 to 1.02 as Re_M is increased from 19 to 40 (Run B30/1). Increasing Re to 200, but keeping $\mathrm{Re}_M = 40$, results in a further increase of $\overline{B}_z^{\rm max}/B_{\rm eq}(z)$ to 1.10 (Run b30/1). This is also an example of a strong flux concentration with $\Pr_M = 0.2$; cf. Sect. 3.3. However, when Re_M is increased further to 95, $\overline{B}_z^{\rm max}/B_{\rm eq}(z)$ decreases to about 0.71; see Table 4. Again, the weakening of the spot might be a consequence of the domain not being deep enough. Alternatively, it could be related to the occurrence of small-scale dynamo action, which is indicated by the fact that in deeper layers the small-scale magnetic field is enhanced in the run with the largest value of Re_M; see
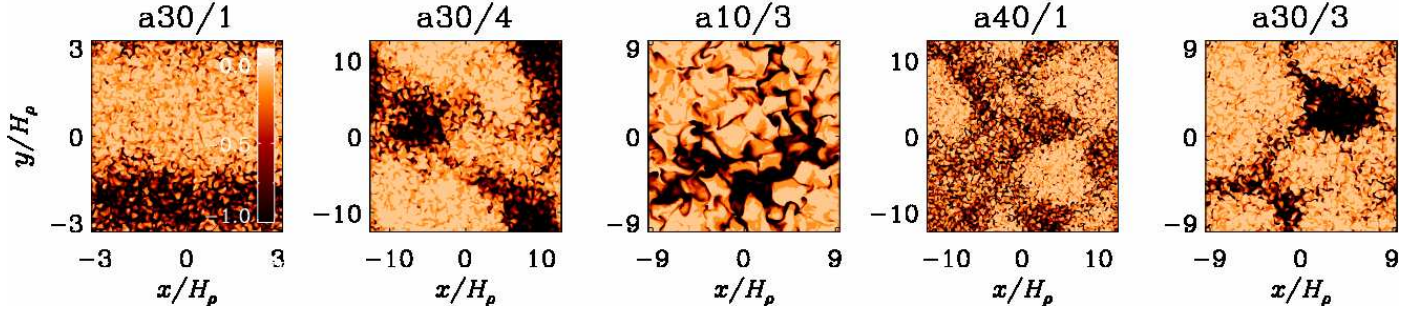
Fig. 15. Magnetic field configuration at the upper surface for DNS Runs a30/1–a30/3 of Table 5.

Table 5. Summary of DNS at varying $\hat{k}_f = k_f/k_1$, $\tilde{k}_f = k_f H_\rho$, $\hat{g} = g/c_s^2 k_1$, and fixed values of $\tilde{B}_0 = 0.02$, $\tilde{\eta}_0 = 2 \times 10^{-4}$, using resolutions of 256^3 mesh points (for Run a30/1), 512^3 mesh points (for Run a30/4, a10/3, and a30/3), as well as $1024^2 \times 384$ mesh points (for Runs a40/1 and A40/1).

Run	Pr_M	Re_M	Ma	$\hat{k}_f$	$\tilde{k}_f$	$\hat{g}$	$\hat{\lambda}$	$\hat{B}_z$	$\hat{\bar{B}}_z$
a30/1	1.0	16	0.09	30	30	1	0.94	3.09	0.78
a30/4	1.0	21	0.13	30	7.5	4	0.18	4.42	0.88
a10/3	1.0	63	0.13	10	3.4	3	—	4.83	0.40
a40/1	1.0	33	0.07	40	10	1	0.83	3.83	0.87
A40/1	1.0	33	0.07	40	10	1	1.05	5.81	1.41
a30/3	0.5	23	0.14	30	10	3	0.46	4.47	1.31

Fig. 13. In Run C30/1 with the largest value of Re_M, the spot is larger and more fragmented, but it still remains in place and statistically steady; see Fig. 14 and http://www.nordita.org/~brandenb/movies/NEMPI/ for corresponding animations.

3.5. Dependence on scale separation and stratification

We have performed various sets of additional simulations where we change $\hat{g}$ and/or $\hat{k}_f$; see Table 5 and Fig. 15. In those cases, the vertical extent of the domain is from $-\pi$ to 0. As discussed in Sect. 3.1 this might be too small in some cases for NEMPI to develop fully. Nevertheless, in all cases there are clear indications for the occurrence of flux concentrations. The results regarding the growth rate of NEMPI are not fully conclusive, because the changes in k_f and H_ρ also affect turbulent–diffusive and turnover time scales. As shown in the appendix of Kemel et al. (2013) the normalized growth rate of NEMPI is given by:

$$\hat{\lambda} + 1 = 3\beta_\star (k_f H_\rho)/(k_\perp H_\rho)^2, \tag{30}$$

which is not changed significantly for a vertical magnetic field; see Sect. 2.1. If $k_\perp H_\rho = \text{const} \approx 0.7$, as suggested by the MFS of Sect. 2.4, we would expect $\hat{\lambda} + 1$ to be proportional to $k_f H_\rho$, which is not in good agreement with the simulation results.

To shed some light on this, we now discuss horizontal power spectra of $B_z(x, y)$ taken at the top of the domain. These spectra are referred to as $E_M^z(k)$ and are normalized by B_{eq}^2/k_f. In Run a30/4 with $\hat{g} = 4$ and $\hat{k}_f = 30$, we have access to wavenumbers down to $k_1 H_\rho = 0.25$. The results in Fig. 16 show that there is significant power below $k_\perp H_\rho = 0.7$. This is in agreement with the MFS in the nonlinear regime; see Fig. 3. The time
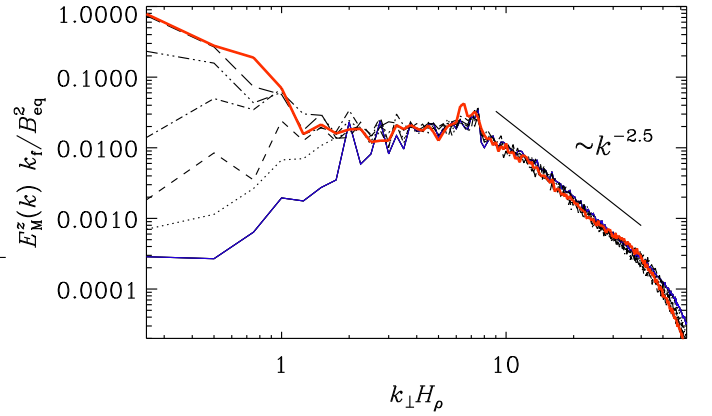

Fig. 16. Normalized spectra of B_z from DNS Run a30/4 at normalized times $t\eta_{t0}/H_\rho^2 \approx 0.2, 0.5, 1, 2, 5, 10,$ and 20, for $\hat{g} \equiv g/c_s^2 k_f = 4$.
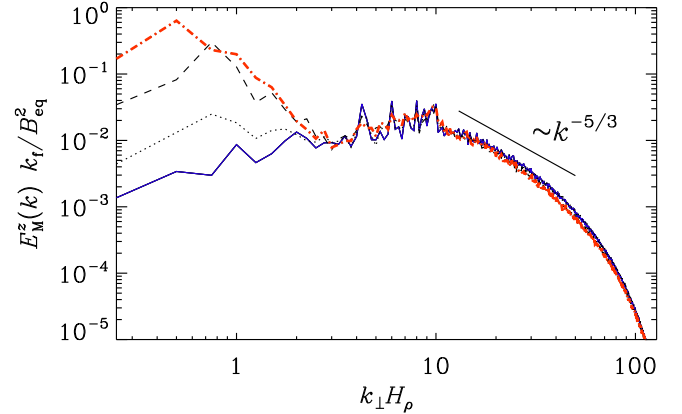

Fig. 17. Normalized spectra of B_z from DNS Run A40/1 at normalized times $t\eta_{t0}/H_\rho^2 \approx 0.2, 0.5, 1,$ and 2.7 with $k_f H_\rho = 10$ and $k_1 H_\rho = 0.25$.

evolution of $E_M^z(k)$ suggest a behavior similar to that of an inverse magnetic helicity cascade that was originally predicted by (Frisch et al., 1975) and later verified both in closure calculations (Pouquet et al., 1976) and DNS (Brandenburg, 2001). Similar results with inverse spectral transfer are shown in Fig. 17 for DNS Run A40/1. The only difference between Runs A40/1 and a40/1 is the vertical extent of the domain, which is twice as tall in the former case ($3\pi H_\rho$ instead of $1.5\pi H_\rho$). We note in this connection that the spectra tend to show a local minimum near $k_f/6$. This justifies our earlier assumption of separating mean and fluc-
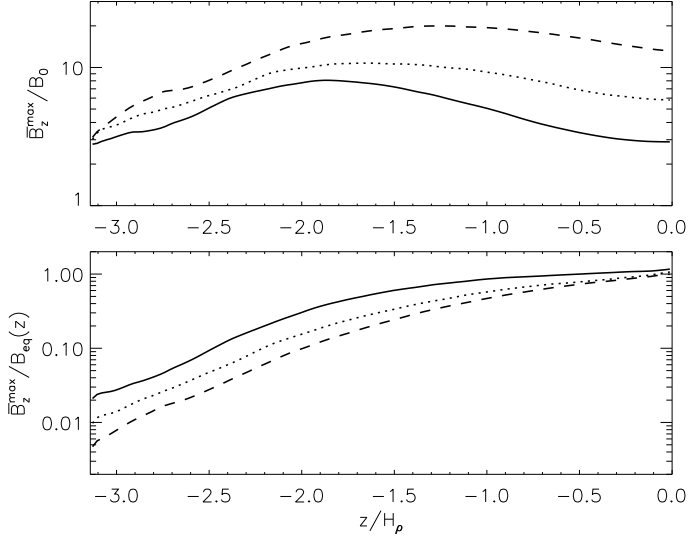
Fig. 18. Same as Fig. 12, but for the ILES runs with varying forcing amplitude. Note the different vertical extent of this set of models. The different lines indicate Ma = 0.16 (solid), 0.34 (dotted), and 0.68 (dashed).
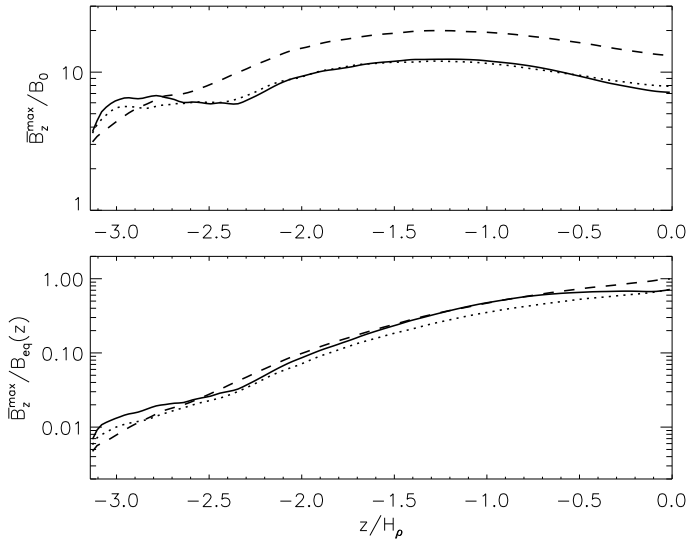
Fig. 19. Same as Fig. 18, but for the ILES runs which vary both the forcing amplitude and the imposed magnetic field at the same time, keeping the *relative* field strength comparable. The different lines again indicate Ma = 0.16 (solid), 0.35 (dotted), and 0.68 (dashed), and agree markedly well in the lower panel where we plot relative to $B_{\mathrm{eq}}(z)$.

tuating fields at the wavenumber $k_{\mathrm{f}}/6$; see Sect. 3.1. The spectra also show something like an inertial subrange proportional to $k^{-5/3}$ (Fig. 17) or $k^{-2.5}$ (Fig. 16). The latter is close to the k^{-3} subrange in the MFS of Fig. 3. Those steeper spectra could be a symptom of a low Reynolds number or, alternatively, a consequence of most of the energy inversely 'cascading' to larger scales in the latter two cases.

We also checked how different kinds of helicities vary during NEMPI. In the present case, magnetic and kinetic helicities are fluctuating around zero, but cross helicity is not. The latter is an ideal invariant of the hydromagnetic equations, but in the present case of a stratified layer with a vertical net magnetic field, $\langle \boldsymbol{u} \cdot \boldsymbol{b} \rangle$

Table 6. Summary of DNS and ILES at varying values of Ma, all for $\hat{g} = 3$, $\hat{k}_{\mathrm{f}} = 30$. For ILES, no accurate values of $\hat{\lambda}$ are available. In the DNS, the resolution is 256^2 for Runs D01 and D02, and 512^2 for Run D10, while for Runs I03–I30 it is $256^2 \times 128$.

Run	$\tilde{B}_0$	Re$_M$	Ma	$\hat{\lambda}$	$\hat{B}_z$	$\hat{\tilde{B}}_z$
D01	0.01	24	0.15	0.28	3.06	0.78
D02	0.02	24	0.14	0.46	4.47	1.31
D10	0.10	8	0.50	0.25	4.91	1.61
I03	0.10	—	0.16	>1	2.86	1.14
I10	0.10	—	0.34	>1	2.70	1.00
I30	0.10	—	0.68	>1	2.41	1.02

can actually be produced; see Rüdiger et al. (2011), who showed that

$$\langle \boldsymbol{u} \cdot \boldsymbol{b} \rangle \approx \eta_{\mathrm{t}} \boldsymbol{g} \cdot \boldsymbol{B}_0 / c_{\mathrm{s}}^2 = -\eta_{\mathrm{t}} B_0 / H_\rho. \tag{31}$$

In a particular case of Run 30/1, we find a time-averaged value of $\langle \boldsymbol{u} \cdot \boldsymbol{b} \rangle$ that would suggest that $\eta_{\mathrm{t}}/\eta_{\mathrm{t}0}$ is around 6, which is significantly larger than unity. This would agree with independent arguments in favor of having underestimated η_{t}; see the discussion in Sect. 2.5. In other words, if η_{t} were really larger than what is estimated based on the actual rms velocity, it would also explain why the diameter of tubes is bigger in the DNS than in the MFS.

3.6. Mach number dependence

To study the dependence on Mach number, it is useful to consider ILES without any explicit viscosity or magnetic diffusivity. In Figs. 18–20 we show the results for three values of Ma at $\hat{g} = gk_1/c_{\mathrm{s}}^2 = 3$ and $\hat{k}_{\mathrm{f}} = k_{\mathrm{f}}/k_1$ using a resolution of $256^2 \times 128$ nodes on the mesh. In Table 6 we give a summary of various output parameters and compare with corresponding DNS. Note first of all that the results from ILES are generally in good agreement with the DNS. This demonstrates that the mechanism causing magnetic flux concentrations by NEMPI is robust and not sensitive to details of the magnetic Reynolds number, provided that Re$_M > 10$. The normalized growth rate is in all three cases above unity.

As the Mach number is increased, the magnetic structures become smaller; seen in the left-hand panels of Fig. 20. Since the properties of NEMPI depend critically on the ratio $\overline{B}/B_{\mathrm{eq}}$, and since $B_{\mathrm{eq}}(z)$ and hence $B_{\mathrm{eq}0}$ increase with increasing Mach number, the decrease in the size of magnetic structures might just reflect the fact that for smaller values of $\overline{B}/B_{\mathrm{eq}0}$, NEMPI would operate at higher layers which are no longer included in our computational domain. Looking at Fig. 18, it is clear that the maximum of $\overline{B}/B_0$ moves to higher layers, but it is still well confined within the computational domain. Nevertheless, if one compensates for the decrease of B_{eq} by applying successively weaker mean fields when going to lower Mach number (right-hand panels of Fig. 20), the size of the emerging structures remains approximately similar and the curves of $\overline{B}/B_{\mathrm{eq}}$ lie now nearly on top of each other. This shows clearly that in our simulations with Ma ≈ 0.7, flux concentrations are well possible. This is important, because it allows for the possibility that the energy density of magnetic flux concentrations can become comparable with the thermal energy.
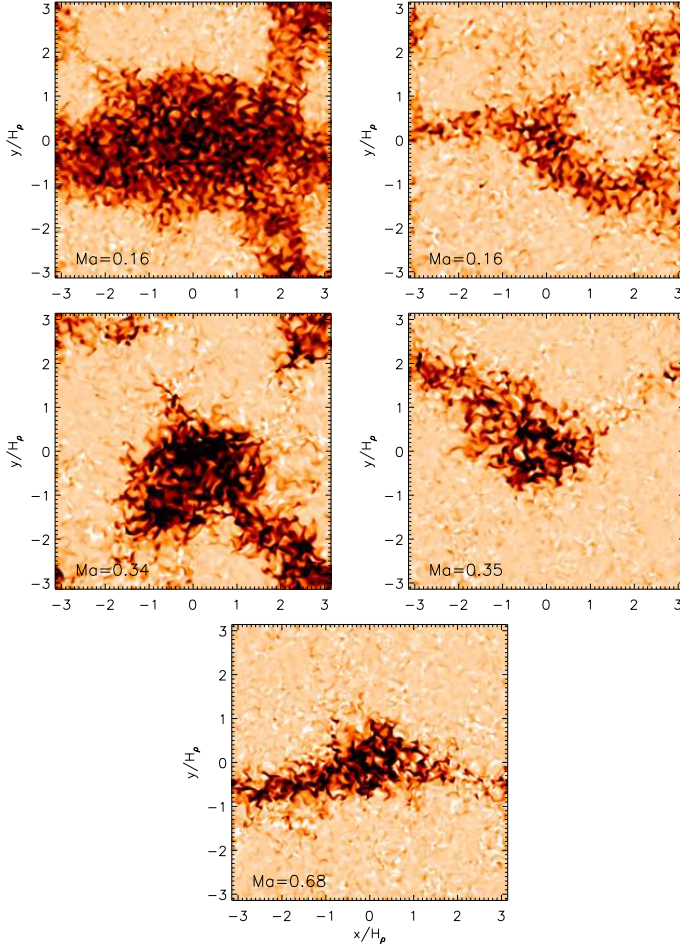
Fig. 20. Surface appearance of the vertical magnetic field, B_z^{max}, in the ILES simulations with different Mach numbers (top to bottom). The color coding shows $B_z^{\mathrm{max}}/B_{\mathrm{eq}}$ in the range of -0.1 (white) to $+1.0$ (black). Root-mean-square Mach numbers are given by the labels. For the upper two rows with lower Mach number, the left column is for fixed initial mean field, whereas in the right column the initial field is adjusted between the runs, such that the field strength remains constant relative to the kinetic energy in the background turbulence.

4. Conclusions

Using DNS, ILES and MFS in a wide range of parameters we have demonstrated that an initially uniform vertical weak magnetic field in strongly stratified hydromagnetic turbulence with large scale separation results in the formation of circular magnetic spots of equipartition and super-equipartition field strengths. Although we have confirmed that the normalized horizontal wavenumber of magnetic flux concentrations is $k_\perp H_\rho \approx 0.8$, as found earlier for horizontal imposed field (Kemel et al., 2013), it is now clear that in the nonlinear regime smaller values can be attained. This happens in a fashion reminiscent of an inverse cascade or inverse transfer in helically forced turbulence (Brandenburg, 2001). (Since in both the transfer is nonlocal in wavenumber space, we avoid talking about cascade in favor of transfer.) In the present case, this inverse transfer is found both in MFS and in DNS. This property helps explaining the possibility of larger length scales separating different flux concentrations.

The study of axisymmetric MFS helps understanding the dependence of NEMPI on the parameters $\beta_\star$ and β_{p} which determine the parameterization of the effective magnetic pressure,

$\mathcal{P}_{\mathrm{eff}}(\beta)$. It was always clear that changes in those parameters can significantly change the functional form of $\mathcal{P}_{\mathrm{eff}}(\beta)$, and yet the resulting growth rate of NEMPI was found to depend mainly on the value of $\beta_\star$. We now see, however, that the shape of the resulting solutions still depends on the value of $\beta_\star$, in addition to a dependence on β_{p}. In fact, smaller values of β_{p} as well as larger values of $\beta_\star$ both result in longer structures. This is important background information in attempts to find flux concentrations in DNS, where the domain might not always be tall enough. As a rule of thumb, we can say that the domain is deep enough if the resulting large-scale magnetic field is below 1% of the equipartition value. This is confirmed by Figs. 12 and 13 as well as Figs. 18 and 19, where all runs with $\overline{B}_z^{\mathrm{max}}/B_{\mathrm{eq}}(z) \leq 0.01$ at $z = z_{\mathrm{bot}}$ reach $\overline{B}_z^{\mathrm{max}}/B_{\mathrm{eq}}(z) = O(1)$ at $z = z_{\mathrm{top}}$, provided the domain is also high enough. A limited extent at the top appears to be less critical than at the bottom, because NEMPI still develops in almost the same way as before.

It is important to emphasize that the formation of magnetic flux concentrations is equally well possible at large Mach numbers. This is important in view of applications to the Sun, where in the upper layers Ma ≈ 0.5 can be expected. Nevertheless, our present investigations have not yet been able to address the question whether sunspots can really form through NEMPI. For that, we would need to abandon the assumption of isothermality. Nevertheless, we expect the basic feature of downflows along flux tubes to persist also in that case. It is the associated inflow from the side that keeps the tube concentrated. Such flows have also been seen in local helioseismology (Zhao et al., 2010). Those authors also find an additional outflow higher in the photosphere that is known as the Evershed flow.

We expect that the downflow in the tube plays an important role in an unstably stratified layer, such as in the Sun, where it brings low entropy material to deeper layers, lowering therefore the effective temperature in the magnetic tubes. Future work should hopefully be able to demonstrate that in detail. The conceptual difference between NEMPI and other mechanisms may not always be very clear. However, by using an isothermal layer, we can be sure that convection is not operating. Thus, the phenomenon of flux segregation found by Tao et al. (1998) would not work. Conversely, however, NEMPI might well be a viable explanation for this phenomenon too. Whether the concept of flux expulsion can really serve as an alternative paradigm is unclear, because it is difficult to draw any quantitative predictions from it. In particular, flux expulsion does not make any reference to turbulent pressure or its suppression. Instead, the source of free energy is more directly potential energy which can be tapped through the superadiabatic gradient in convection. By contrast, the source of free energy for NEMPI is turbulent energy. The other possibility discussed above is the network of downdrafts associated with the supergranulation layer (Stein & Nordlund, 2012). This mechanism is not easily disentangled from NEMPI, because both imply flux concentrations in downdrafts. However, in an isothermal layer, we can be sure that supergranulation flows are absent, so NEMPI is the only known mechanism able to explain the flux concentrations shown in the present paper.

References

Brandenburg, A. 2001, ApJ, 550, 824

Brandenburg, A. 2005, ApJ, 625, 539

Brandenburg, A., Kemel, K., Kleeorin, N., Mitra, D., & Rogachevskii, I. 2011, ApJ, 740, L50

Brandenburg, A., Kemel, K., Kleeorin, N., Rogachevskii, I. 2012, ApJ, 749, 179

Brandenburg, A., Kleeorin, N., & Rogachevskii, I. 2013, ApJL, in press, arXiv:1306.4915

Cheung, M. C. M., Rempel, M., Title, A. M., & Schüssler, M. 2010, ApJ, 720, 233

Fan, Y. 2009, Living Rev. Solar Phys., 6, 4

Frisch, U., Pouquet, A., Léorat, J., & Mazure, A. 1975, J. Fluid Mech., 68, 769

Grinstein F. F., Fureby C., DeVore C. R., 2005, IJNMF, 47, 1043

Kemel, K., Brandenburg, A., Kleeorin, N., Mitra, D., & Rogachevskii, I. 2012a, Solar Phys., 280, 321

Kemel, K., Brandenburg, A., Kleeorin, N., Mitra, D., & Rogachevskii, I. 2013, Solar Phys., 287, 293

Kemel, K., Brandenburg, A., Kleeorin, N., & Rogachevskii, I. 2012b, Astron. Nachr., 333, 95

Kitiashvili, I. N., Kosovichev, A. G., Wray, A. A., & Mansour, N. N. 2010, ApJ, 719, 307

Kleeorin, N., & Rogachevskii, I. 1994, Phys. Rev. E, 50, 2716

Kleeorin, N., Mond, M., & Rogachevskii, I. 1993, Phys. Fluids B, 5, 4128

Kleeorin, N., Mond, M., & Rogachevskii, I. 1996, A&A, 307, 293

Kleeorin, N. I., Rogachevskii, I. V., & Ruzmaikin, A. A. 1989, Sov. Astron. Lett., 15, 274

Kleeorin, N. I., Rogachevskii, I. V., & Ruzmaikin, A. A. 1990, Sov. Phys. JETP, 70, 878

Losada, I. R., Brandenburg, A., Kleeorin, N., & Rogachevskii, I. 2013, A&A, 556, A83

Pouquet, A., Frisch, U., & Léorat, J. 1976, J. Fluid Mech., 77, 321

Rempel, M. 2011, ApJ, 740, 15

Rogachevskii, I., & Kleeorin, N. 2007, Phys. Rev. E, 76, 056307

Rüdiger, G., Kitchatinov, L. L., & Brandenburg, A. 2011, Solar Phys., 269, 3

Rüdiger, G., Kitchatinov, L. L.& Schultz, M. 2012, Astron. Nachr., 333, 84

Spruit, H. C. 1979, Solar Phys., 61, 363

Spruit, H. C. 1981, A&A, 102, 129

Sur, S., Brandenburg, A., & Subramanian, K. 2008, MNRAS, 385, L15

Stein, R. F., & Nordlund, Å. 2012, ApJ, 753, L13

Tao, L., Weiss, N. O., Brownjohn, D. P., & Proctor, M. R. E. 1998, ApJ, 496, L39

Warnecke, J., Losada, I. R., Brandenburg, A., Kleeorin, N., & Rogachevskii, I. 2013, ApJ, submitted, arXiv:1308.1080

Zhao, J., Kosovichev, A. G., Sekii, T. 2010, ApJ, 708, 304

Ziegler U., 2004, J. Comput. Phys., 196, 393